Supporting information

1 **Negative Space Charge Modulated Ion Transport through**

2 **PEDOT: PSS Hydrogel Integrating Nanofluidic Channels for**

3 **High-Efficient Osmotic Energy Harvesting**

4 Rui Zhu,[a] Peng Sun,[d] Guofeng Cui,[a*] Yaoguang Yu,[b*] Shaojun Ke,[c] Jie Zhao,[c]

5 [a.] *Key Laboratory for Polymeric Composite & Functional Materials of Ministry of Education, Key Laboratory of Low-carbon Chemistry &*

6 *Energy Conservation of Guangdong Province, School of Chemistry, Sun Yat-sen University, Guangzhou 510275, P. R. China. E-mails:*

7 *cuigf@mail.sysu.edu.cn.*

8 [b.] *School of Materials, Sun Yat-sen University, Shenzhen 518107, P. R. China. E-mails: yuyg5@mail.sysu.edu.cn.*

9 [c.] *School of Mechanical and Automotive Engineering, South China University of Technology, Guangzhou 510640, P. R. China.*

10 [d.] *Guangdong Provincial Engineering Technology Research Center of Vacuum Coating Technologies and New Energy Materials, Siyuan*

11 *Laboratory, Guangzhou Key Laboratory of Vacuum Coating Technologies and New Energy Materials, Department of Physics, Jinan*

12 *University, Guangzhou, Guangdong 510632, People's Republic of China.*

13

14 **Experimental Methods**

15   To further verify the effect of the thickness and composition (PEDOT: PSS) of the hydrogel

16 membrane on the acquisition of osmotic energy, different single-factor experiments were executed

17 separately. Firstly, hydrogel membranes of 100 µm, 200 µm, 300 µm, 400 µm, 500 µm, and 600

18 µm sizes were prepared and assembled into the osmotic energy acquisition device to verify the effect

19 of membrane thickness on osmotic energy performance with the concentration gradient of artificial

20 seawater and river water, respectively. Then, the thickness of the membrane was fixed at 236 µm,

21 and the effect of PEDOT: PSS addition on the output power was verified by controlling the amount

22 of PEDOT: PSS added (1%, 3%, 5%, 7%, 10%, 15%, 20%, and 25%) with the concentration

23 gradient of artificial seawater and river water.

24

Supporting information
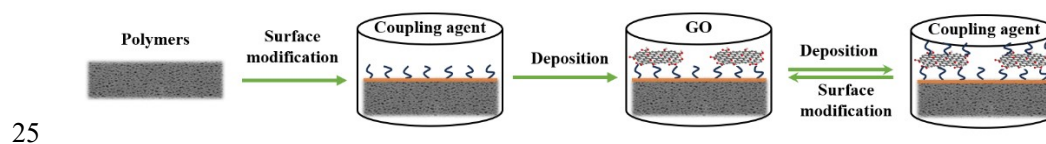
25

26 **Fig. S1** Schematic of synthesis of conventional permeable membrane. The preparation of permeable

27 membranes by composite/ modified polymers with 2D materials was previously considered a viable

28 option, but the complicated process and lower stability posed significant challenges to its advancement.

29

Supporting information
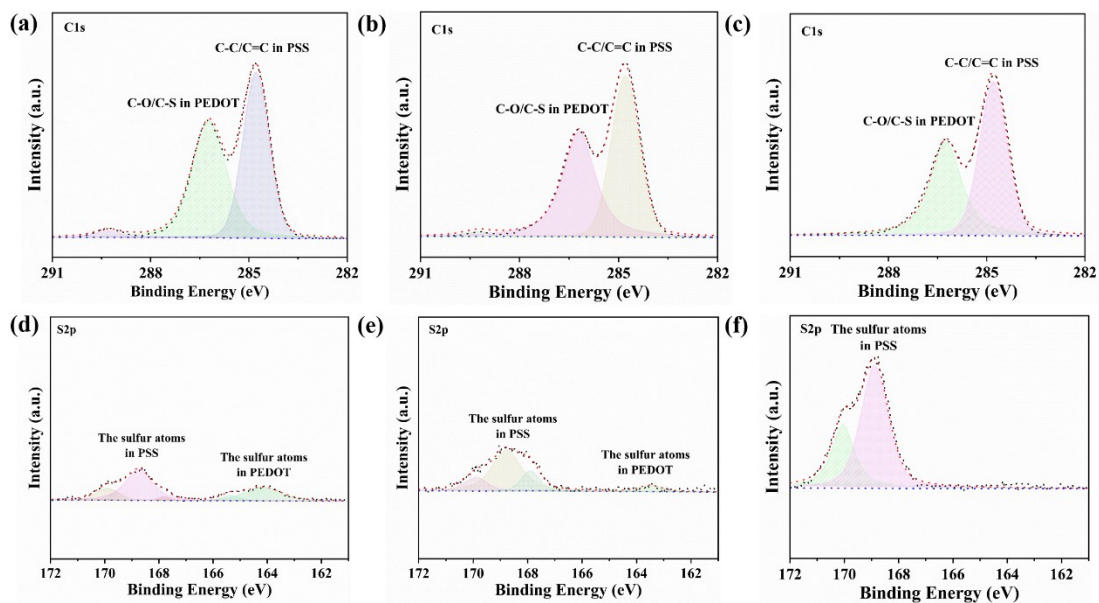
31 **Fig. S2** (a)-(c) C1s XPS spectra and (d)-(f) S2p XPS spectra of PEDOT: PSS hydrogel.

32   As depicted in Fig. 1(b), the shift of the $C\alpha=C\beta$ bond in PEDOT to lower

33 wavelengths, the slight shift of the C-S-C bond (579 cm^{-1}) to shorter wavelengths,

34 coupled with its significant enhancement upon H_2SO_4 doping, which these indicate the

35 increase of quinone structure in the main chain of PEDOT. As shown in Fig. S2(a)-(c),

36 the peak at 284 eV corresponds to the C-C/C=C bond in PSS, while the peak at 286 eV

37 corresponds to the C-O/C-S bond in PEDOT. Obviously, the increased ratio of C-

38 C/C=C to C-O/C-S indicates that more sulfonates in the PSS chain segments form

39 hydrogen bonds with PVA or PA. Meanwhile, in the S(2p) XPS spectra (Fig. S2(d)-

40 (f)), the peaks at 166-172 eV and 161-166 eV were attributed to the sulfur atoms in PSS

41 and PEDOT, respectively. The proportion of sulfur elements in PSS and PEDOT

42 gradually increases with further doping cross-linking, which was attributed to the

43 substitution of partial PSS by PA during the cross-linking process and the doping of

44 H_2SO_4.

45
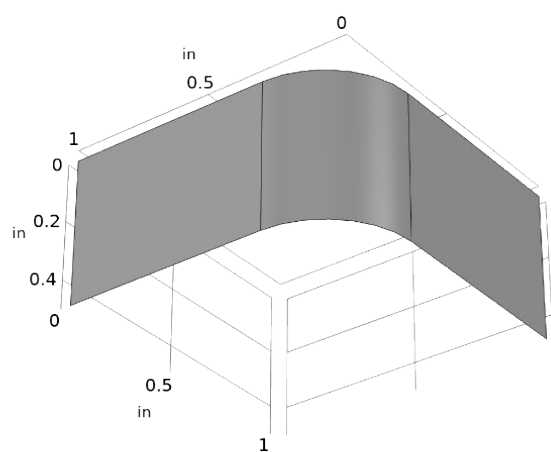
46

47   **Fig. S3** Bending strain analysis model.

48
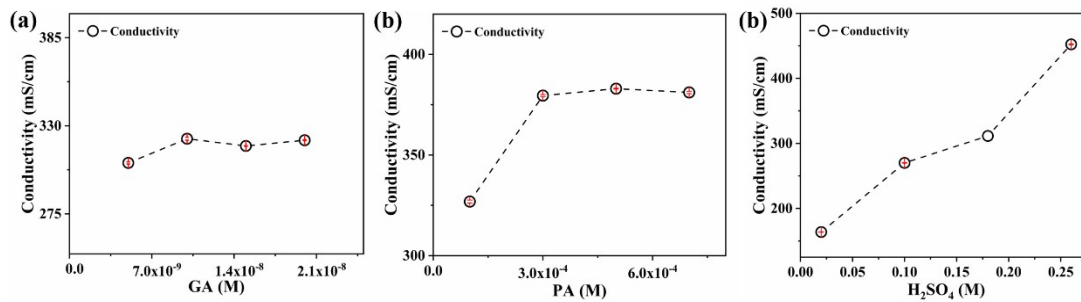
Fig. S4 Conductivity test results of PEDOT: PSS hydrogels adding different amounts of (a) GA, (b) PA and (c) H_2SO_4, respectively.
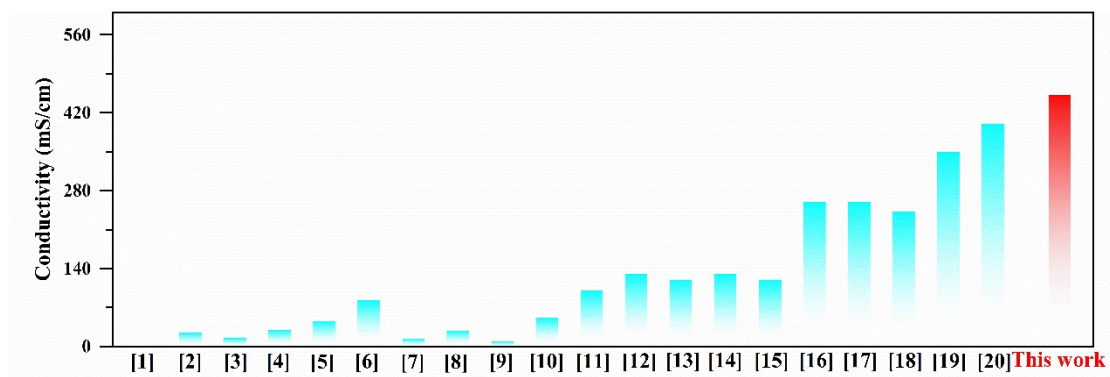
Fig. S5 Comparison of conductivity with the reported composite conductive hydrogels. [1-20]

Supporting information
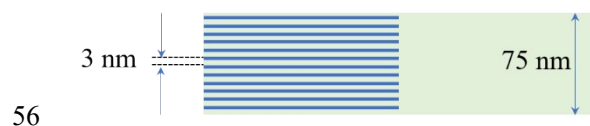
56

57 **Fig. S6** Nano-channel computational modeling.

58

Supporting information

MEASUREMENT OF OSMOTIC ENERGY CONVERSION

59

60   As shown in Fig. 4(f), the whole circuit diagram consists of three parts: the electrode,

61   membrane, and external circuit. Among them, the membrane includes membrane

62   resistance r_{int} and transmembrane diffusion potential. r_{int} denotes the ion transport

63   resistance in the ion-selective membrane. E_{diff} is generated by the concentration

64   gradient on both sides of the membrane, which can be calculated by the following

65   equation:

$$E_{diff} = (2t_+ - 1)\frac{RT}{zF}\ln\left(\frac{\gamma_H C_H}{\gamma_L C_L}\right)$$

66

67   where R is the universal gas constant, T is the Kelvin temperature, z is the ion valence

68   state, and F is the Faraday constant. C_H and C_L are the ion concentrations at high

69   concentrations and low concentrations, respectively. γ_H and γ_L are the ion activity

70   coefficients of the high-concentration solution and low-concentration solution,

71   respectively.

72   The measured V_{OC} is the sum of E_{diff} and E_{redox} as in the following formula:

73   $V_{oc} = E_{diff} + E_{redox}$

74   The electrodes can be abstracted as the redox potential E_{redox}, which is derived from

75   the electrode potential drop when the two electrodes enter solutions of different

76   concentrations. The E_{redox} can be calculated by the following equation:

$$E_{redox} = \frac{RT}{zF}\ln\left(\frac{\gamma_H C_H}{\gamma_L C_L}\right)$$

77

78   The external circuit consists of an external load r_L and an ammeter used to measure

79   the current in the circuit.

Supporting information

Supporting information
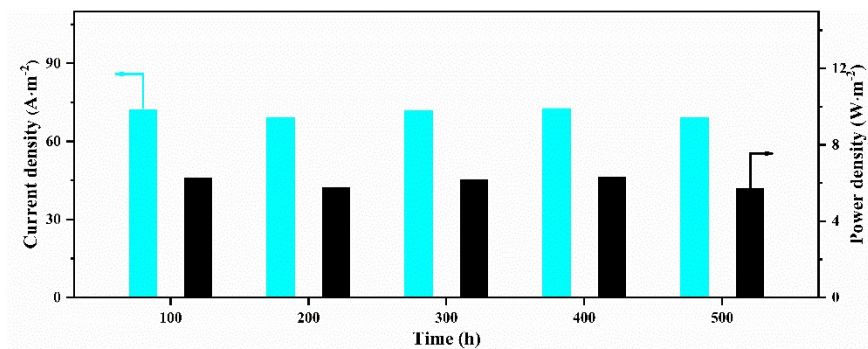
81

82　**Fig. S7** The device stability of power generation.

83

Supporting information
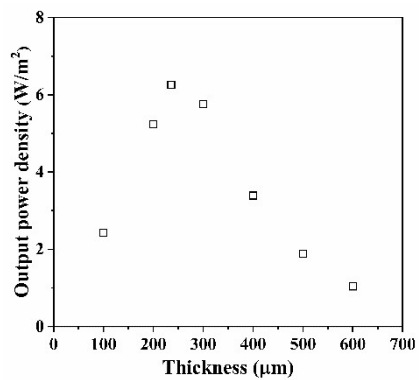
84

85 **Fig. S8** The influence of the hydrogel membrane thickness in osmotic energy performance.

86

Supporting information
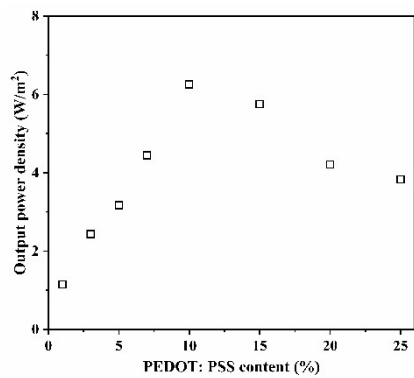
87

88   **Fig. S9** The influence of PEDOT: PSS addition in osmotic energy performance.

89
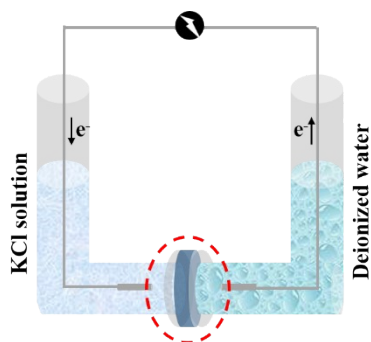
90

91 **Fig. S10** Schematic representation of the ICEG setup.

92 **Table S1** Electrochemical parameters of a single unit of the ICEG.

	V_0 (mV)	V_{theo} (mV)	Permselectivity (%)	Conversion efficiency (%)
Configuration (I)	396	414	95.6	45.8

93　　The parameters of a single unit of the PEDOT: PSS membrane pair were measured

94　in an ICEG device (Fig. S10). Ag/AgCl was used as the cathode and anode. The high

95　concentration (HC) and low concentration (LC) of the salt solutions were 3.0 M and

96　0.3 μM, respectively. The membrane permselectivity (α) could be calculated as the

97　ratio between the measured membrane potential (V_{meas}) and the theoretical membrane

98　potential (V_{theo}): [21, 22]

99
$$\alpha(\%) = \frac{V_{meas}}{V_{theo}} \times 100$$

100
$$V_{theo} = N\frac{RT}{zF}\ln\left(\frac{a_H}{a_L}\right)$$

101　　where N is the number of membranes, α is the average membrane permselectivity of

102　an anion and a cation exchange membrane, R is the universal gas constant (8.314 J·mol⁻

103　¹·K⁻¹), T is the absolute temperature (K), z is the electrochemical valence, F is the

14

Supporting information

104 Faraday constant (96485 C·mol^{-1}), a_H is the activity of the concentrated solution

105 (mol·L^{-1}), and a_L is the activity of the diluted solution (mol·L^{-1}). For seawater (3.0 M

106 KCl) and river water (0.3 μM KCl) the theoretical voltage difference over each

107 membrane for 100% selective membranes is 414 mV.

108   The electrochemical conversion efficiency (η) can be calculated by the following

109 formula: [23, 24]

110
$$\eta_{max} = \frac{\alpha^2}{2}$$

111

Supporting information

112 **Table S2** Comparison of osmotic energy conversion performance.

Material	Solution	Testing area (mm^2)	Energy conversion performance	Ref.
PET membrane	Artificial seawater and river water	0.03	0.86 W/m^2	[54]
PAM hydrogel membrane	Artificial seawater and river water	28	0.37 W/m^2	[55]
SPEEK membranes	Artificial seawater and river water	28	5.8W/m^2	[56]
HEMAP hydrogel membrane	Artificial seawater and river water	0.03	5.38 W/m^2	[57]
Loofah sponge membranes	Artificial seawater and river water	60	0.0183 W/m^2	[58]
MMT membranes	Artificial seawater and river water	0.03	2.1 W/m^2	[59]
KANF membranes	Artificial seawater and river water	0.03	4.8 W/m^2	[60]
GOMs membrane	Artificial seawater and river water	0.03	4.94 W/m^2	[61]
PPC membrane	Artificial seawater and river water	0.075	2.2 W/m^2	[62]

FOF membrane	0.5M/1mM NaCl solution	0.02	5.7 W/m^2	[63]
Glass membrane	Artificial seawater and river water	0.03	4.16 W/m^2	[64]
MMT membranes	Artificial seawater and river water	0.03	4.13 W/m^2	[65]
PEDOT: PSS hydrogel	**Artificial seawater and river water**	**38.5**	**6.26 W/m^2**	**This work**

113   Note: Composition of simulated seawater (NaCl: 0.454M; MgSO$_4$: 0.028M; MgCl$_2$: 0.0257M; CaCl$_2$:

114   0.0103M; KCl: 0.00972M; NaHCO$_3$: 0.00241M) and river water (NaCl: 0.01M).

115

PET plastic
PPPSH
River water
Sea water
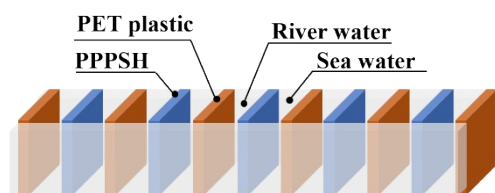
Ion Concentration-induced Electricity Generator

116

117 **Fig. S11** Electrochemical cell series device.

118
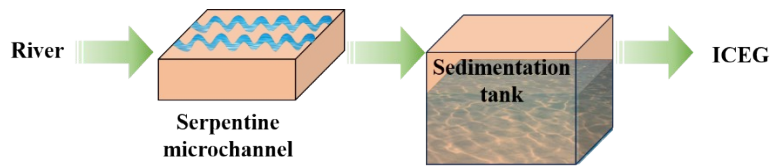
119

120 **Fig. S12** River water pre-treatment unit. In practical application, flowing river water flows into the series-

121 connected ICEG devices through serpentine microchannels and settling tanks, which can effectively

122 buffer the current impact and reduce impurities.

123

River water
Sea water
PET plastic
Hydrogel
Electrode
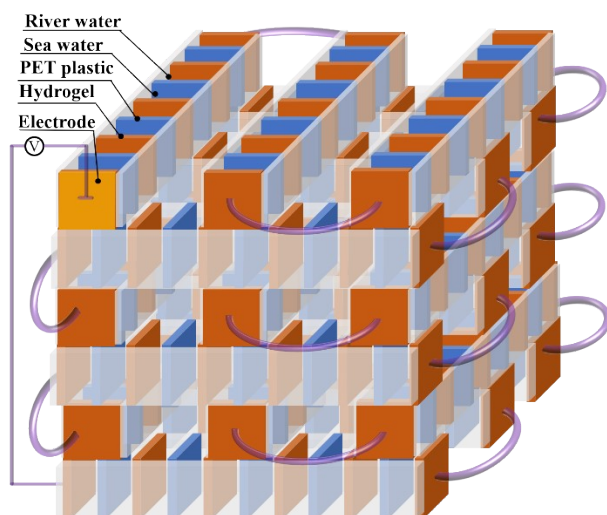
124

125   **Fig. S13** Schematic diagram of ICEG devices.

126
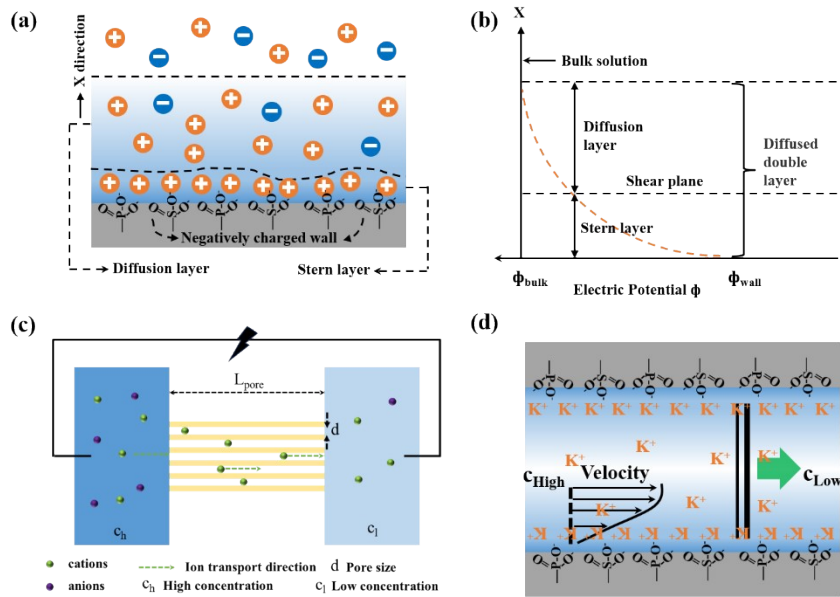
Fig. S14 (a) Schematic diagram of the electrical double layer mechanism (EDL) next to a negatively charged wall. (b) Diffusion-osmotic current induced by salt concentration difference. (c) Sketch of the nanofluidic osmotic energy conversion model. (d) Electrical distribution from charged wall to bulk solution.

We built a two-dimensional model to illustrate the osmotic energy conversion process, as shown in Fig. S14c. The model consists of a high concentration of seawater, a low concentration of river water and a hydrogel nanochannel membrane. In the negatively charged nano-channels, the electrostatic force repels ions with the same charge (co-ions, negatively charged Cl^- ions in our work) near the channel surface and attracts ions with the opposite charge (counter-ions, positively charge K^+ ions in our work) to compensate the fixed charges (in our study negatively charges introduced by sulphuric or phosphoric acid groups) on the surface, thus leading to a charge redistribution. [25] However, only a fraction of counter-ions ends up at the charged wall. A graded electric double-layer (abbreviated as EDL) is created between the nano-channel wall and the electrolyte solution, with an increased concentration of counter-ions and a decreased concentration of co-ions (Fig. S14a). The EDL refers to the Stern and diffusion layers. [26-28]

Supporting information

143   The Stern layer is comprised entirely of counter-ions due to contact interactions. The diffusion layer is

144   the region from the Stern layer to the bulk solution, where the distribution of free ions is still governed

145   by the Coulomb force, electrically screened by the Stern layer. As depicted in Fig. S14b, the interaction

146   between counterions in the nano-channel and the charge of its inner wall is usually simplified by an

147   exponentially decaying potential. [29] Through this interaction, by which way the channel is filled with a

148   close to unipolar solution of counter-ions, and ion selectivity of transport can be observed. Based on the

149   ion-selectivity mechanism, a streaming current is generated when the ionic solution is propelled by an

150   external mechanical driving force (a transmembrane concentration difference) through charged

151   nanofluidic channels (Fig. S14d). [30-34] In this way, the net charge (counter-ions, K^+ in our work) within

152   the diffused double layer moves at a certain velocity under the effect of a concentration gradient. At this

153   point, counter-ions (K^+ ions in this work) spontaneously and preferentially diffuse along the diffused

154   double layer within the nano-channels. Ideally, the transport of counter-ions is proportional to the charge

155   density on the surface of the nano-channel. Conductance measurements reveal the charge-control ion

156   transportation within the PEDOT: PSS hydrogel membrane, as shown in Fig. 3(c), where the measured

157   ionic conductance exhibited two distinct characteristic behaviors. [35] Specifically, above the 0.5M

158   concentration point, the ionic conductance of the membrane follows the bulk rule of linearly increasing

159   with concentration. However, the conductance deviates from the bulk value and gradually approached

160   smoothing at concentrations less than 0.5M. In the low concentration region, the selective transport of

161   ions tends to be controlled by the double electric layer within the nano-channel, as depicted in Fig. S14d.

162   Because of the negatively charged surface in the channel (the intrinsic negative charge of the nano-

163   channel inner wall is introduced by sulfate or phosphate groups during the synthesis of the hydrogel), K^+

164   ions with opposite charges will be separated from identically charged Cl⁻ ions in the channel, creating a

165   unipolar environment.

166

Supporting information

167 **Table S3** Price Comparison of Permeable Membranes.

Membrane	Component	Functional Group	Size for single sheet	Price
AMI-7001S anion exchange membrane [a]	Gel polystyrene cross linked with divinylbenzene	Quaternary Ammonium	1.2 m × 1.0 m × 0.45 mm	$350 per sheet
CMI-7000S cation exchange membrane [a]	Gel polystyrene cross linked with divinylbenzene	Sulphonic Acid	1.2 m × 1.0 m × 0.45 mm	$350 per sheet
PEDOT: PSS membrane	PEDOT: PSS hydrogel	Phytic Acid PSS	1.2 m × 1.0 m × 1.0 mm	$10 per sheet

168 [a] The commercial ion exchange membranes were provided by Membrane International Inc.

169

Supporting information

References

1. W. H. Shi, Z. W. Wang, H. Song, Y. Z. Chang, W. J. Hou, Y. P. Li, G. Y. Han, *ACS Appl. Mater. Interfaces*, 2022, **14**, 35114-35125.

2. S. T. Wang, G. Q. Guo, X. X. Lu, S. M. Ji, G. X. Tan, L. Gao, *ACS Appl. Mater. Interfaces*, 2018, **10**, 19133-19142.

3. S. M. Zhang, Y. H. Chen, H. Liu, Z. T. Wang, H. N. Ling, A. Khademhosseini, *Adv. Mater.* 2020, **32**, 1904752.

4. Y. Xu, P. A. Patsis, S. Hauser, J. Pietzsch, Y. X. Zhang, *Adv. Sci.* 2019, **6**, 1802077.

5. L. V. Kayser, M. D. Russell, D. Rodriquez, S. N. Abuhamdieh, D. J. Lipomi, *Chem. Mater.* 2018, **30**, 4459-4468.

6. J. N. Arthur, S. Burns, C. M. Cole, Q. T. Barthelme, S. D. Yambem, *J. Mater. Chem. C* 2022, **10**, 13964.

7. N. M. Badawi, M. Bhatia, S. Ramesh, K. Ramesh, B. Shaik, S. F. Adil, *Polymers* 2023, **15**, 571.

8. Q. Wu, J. J. Wei, B. Xu, X. H. Liu, H. B. Wang, W. Wang, Q. G. Wang, W. G. Liu, *Scientific Reports* 2017, **7**, 41566.

9. B. Y. Lu, H. Yuk, S. T. Lin, N. N. Jian, K. Qu, J. K. Xu, X. H. Zhao, *NATURE COMMUNICATIONS* 2019, **10**, 1043.

10. K. Ren, Y. Cheng, C. Huang, R. Chen, Z. Wang, J. Wei, *J. Mater. Chem. B* 2019, **7**, 5704.

11. J. S. Chen, J. F. Liu, T. Thundat, H. B. Zeng, *ACS Appl. Mater. Interfaces* 2019, **11**, 18720-18729.

12. J. Q. Han, Q. Q. Ding, C. T. Mei, Q. L. Wu, Y. Y. Yue, X. W. Xu, *Electrochimica Acta* 2019, **318**, 660-672.

13. T. Wang, Y. Zhang, Q. C. Liu, W. Cheng, X. R. Wang, L. J. Pan, H. X. Xu, *Adv. Funct. Mater.* 2018, **28**, 1705551.

14. J. S. Chen, Q. Y. Peng, T. Thundat, H. B. Zeng, *Chem. Mater.* 2019, **31**, 4553-4563.

15. Y. Shi, M. Wang, C. B. Ma, Y. Q. Wang, X. P. Li, G. H. Yu, *Nano Lett.* 2015, **15**,

Supporting information

199   6276-6281.

200 16. M. Kotal, S. K. Srivastava, B. Paramanik, *J. Phys. Chem. C* 2011, **115**, 1496-1505.

201 17. Z. X. Deng, Y. Guo, X. Zhao, P. X. Ma, B. L. Guo, *Chem. Mater.* 2018, **30**, 1729-
202   1742.

203 18. C. Qian, T. Higashigaki, T. Asoh, H. Uyama, *ACS Appl. Mater. Interfaces* 2020,
204   **12**, 27518-27525.

205 19. J. S. Chen, Q. Y. Peng, T. Thundat, H. B. Zeng, *Chem. Mater.* 2019, **31**, 4553-
206   4563.

207 20. F. F. Fu, J. L. Wang, H. B. Zeng, J. Yu, *ACS Materials Lett.* 2020, **2**, 1287-1301.

208 21. E. Guler, R. Elizen, D. A. Vermaas, *J. Membr. Sci.* 2013, **446**, 266-276.

209 22. P. Dlugolecki, A. Gambier, K. Nymeijer, *Environ. Sci. Technol.* 2009, **43**, 6888-
210   6894.

211 23. J. Ji, Q. Kang, Y. Zhou, *Adv. Funct. Mater.* 2017, **27**, 1603623.

212 24. D. K. Kim, C. H. Duan, Y. F. Chen, *Microfluid. Nanofluid.* 2010, **9**, 1215-1224.

213 25. A. S. Dukhin, P. J. Goetz, *Studies in Interface Science*, 2010, **24**, 21-89.

214 26. D.C. Grahame, *Chem. Rev.*, 1947, **41**, 441-501.

215 27. P. Delahay, *John Wiley & Sons Inc*, 1965.

216 28. M. A. Brown, A. Goel, Z. Abbas, *Angew. Chem. Int. Ed.*, 2016, **55**, 3790-3794.

217 29. W. Sparreboom, A. van den Berg, J. C. Eijkel, *Nat. Nanotechnol.*, 2009, **4**, 713-
218   720.

219 30. F. H. Van der Heyden, D. Stein, C. Dekker, *Phys. Rev. Lett.*, 2005, **95**, 116104.

220 31. F. H. J. Van der Heyden, D. J. Bonthuis, D. Stein, C. Meyer, C. Dekker, *Nano*
221   *Lett.*, 2006, **6**, 2232-2237.

222 32. W. Guo, L. Cao, J. Xia, F. Q. Nie, W. Ma, J. Xue, Y. Song, D. Zhu, Y. Wang, L.
223   Jiang, *Adv. Funct. Mater.*, 2010, **20**, 1339-1344.

224 33. C. L. Rice, R. Whitehead, *J. Phys. Chem.*, 1965, **69**, 4017-4024.

225 34. H. Daiguji, P. Yang, A. J. Szeri, A. Majumdar, *Nano Lett.*, 2004, **4**, 2315-2321.

226 35. W. W. Xin, Z. Zhang, X. Y. Kong, L. Jiang, L. P. Wen, *Nature Communications*,
227   2019, **10**, 3876.